

DESIGN AND UTILIZATION OF THE STANFORD VISION-BASED NAVIGATION TESTBED FOR SPACECRAFT RENDEZVOUS

Connor Beierle*, Joshua Sullivan[†], and Simone D’Amico[‡]

Vision-based navigation is an enabling technology for the new generation of on-orbit servicing and debris-removal missions. In contrast to legacy metrology systems such as radar, lidar, and the global positioning system, vision sensors are passive, simple, and do not place stringent requirements on the spacecraft design in terms of power, weight, or inter-satellite communication. Most importantly, vision-based navigation has the potential to support accurate autonomous relative operations from hundreds of kilometers down to virtually zero separation in many orbit regimes. The demonstration of this capability calls for a new testbed capable of stimulating cameras in a representative sensing environment to assess functionality, performance, and robustness of the navigation tasks before deployment in space. Based on typical requirements posed by future autonomous rendezvous missions, the goal of this research is to design a virtual-reality sensor-in-the-loop optical stimulator with ten-arcseconds angular resolution and over eight orders of magnitude in radiometric dynamic range. This paper addresses the key challenges in the design, development, calibration, verification, and utilization of such an optical stimulator. A rendezvous hardware-in-the-loop simulation is then conducted to verify the functionality and performance of a new optical angles-only navigation article. This test demonstrates a successful estimation and recovery of the relative translational state of a non-stellar object using optical angles-only measurements to within 1% of the ground-truth. Successful verification of this navigation algorithm in the presence of highly variable illumination conditions illustrate the value and potential of the optical stimulator.

INTRODUCTION

Vision-based sensors (VBS) are a ubiquitous part of the satellite navigation system. Common sensors used for inertial navigation are star trackers (ST), Sun and Earth sensors. These sensors are also extensively used for spacecraft relative navigation and in recent years have been extended to facilitate autonomous rendezvous and proximity operations.^{1,2} Examples of such applications are abundant in the distributed space systems community (Orion,³ mDOT,⁴ Exo-S,⁵ CPOD,⁶ AVANTI,¹ ARGON,¹ etc.). Relative vision-based navigation techniques can be applied at inter-spacecraft separations ranging from hundreds of kilometers down to virtually zero separation in many orbit regimes. At large separation distances, the relative motion between spacecraft can be determined using angles-only navigation, which has been considered in several research studies.⁷⁻¹³ In this navigation mode, the observer spacecraft is attempting to estimate the relative orbital motion of a target space object using only optical bearing angles obtained by the VBS. At close range, pose estimation algorithms can be used to estimate relative position, velocity, attitude, and other parameters of a target space object from a single image. Close-range VBS pose estimation algorithms can utilize known visual markers and/or computer aided models of the space object to estimate the relative position and orientation.¹⁴⁻¹⁷

Testing VBS on ground has become of increasing importance for a variety of reasons. One reason is due to a paradigm shift occurring in the new space era, with miniaturization, increasing autonomy, and mass production of satellites necessitating the ability to verify VBS reliably and more efficiently. Future missions with

*Ph.D. Candidate, Aeronautics and Astronautics Department, Stanford University, 496 Lomita Mall, Stanford CA 94305

[†]Ph.D. Candidate, Aeronautics and Astronautics Department, Stanford University, 496 Lomita Mall, Stanford CA 94305

[‡]Assistant Professor, Aeronautics and Astronautics Department, Stanford University, 496 Lomita Mall, Stanford CA 94305

autonomous vehicles are increasing the range of operations and imposing demanding angular and radiometric sensor detection requirements on the vision-navigation payload. Examples of these missions include on-orbit servicing,^{18,19} near Earth object exploration,^{20,21} space situational awareness,²² and many more. In addition, there is great interest in the engineering community in vision-based navigation systems capable of bridging the gap between far- and close-range navigation techniques. This gap comprises mixed navigation modes (i.e. performing inertial and far-range relative navigation simultaneously), transitions between navigation modes (i.e. transition from far- to close-range relative navigation) and highly-variable modes (i.e. optical navigation at highly varying separation and illumination conditions). For example, the long range VBS used on the Autonomous Rendezvous demonstration using GPS and Optical Navigation (ARGON) experiment conducted in the framework of the PRISMA (OHB) mission suffered from blooming when the resident space object was in view, which impacts the quality of its inertial and relative navigation solution.¹ Before the next generation of vision-based navigation systems can be deployed in space, a high-fidelity, high-dynamic-range testbed is necessary to properly verify algorithms, software and hardware in terms of functionality, performance, and robustness.

Spaceborne VBS navigation testing facilities have historically been designed to calibrate and assess only ST.²³⁻²⁶ Typically, a testbed consists of a static star field and corrective optics to account for the finite distance between the optical stimulator (OS) and the camera. These systems typically have limited geometrical imaging precision, radiometric dynamic range, contrast ratio and lack the appropriate software to simulate stellar objects (SO) and non-stellar objects (NSO) in real-time and closed-loop. With these limitations in mind, it is evident that advancements to a laboratory testing environment are necessary to verify the next generation of spaceborne vision-based navigation systems.

This introduction is followed by a literature review, which seeks to identify state of the art VBS testing facilities with the intent of building off the work of others. Following this literature review, a set of functional and performance requirements are established to steer the testbed design process. A summary of the OS geometric and radiometric calibration is then presented. It will be demonstrated that a fully calibrated system is capable of positioning a point source of light to within tens of arcseconds of angular accuracy over eight orders of radiometric magnitude. Two hardware-in-the-loop (HIL) experiments are conducted to simulate dynamic inertial and relative navigation scenarios. Results are analyzed and discussed prior to the conclusions and way forward. Note that although the OS is capable of simulating inertial, far- and close-range relative navigation scenarios, this paper will limit its analysis of results relating only to inertial and far-range relative navigation simulations.

LITERATURE REVIEW

Facilities which have developed the ability to stimulate VBS in a spacecraft attitude determination context have to date, primarily focused on simulating star fields used for inertial navigation sensors. Several of these facilities are briefly summarized in Table 1.

Table 1: Summary of HIL testbeds used to stimulate VBS for inertial and/or relative spaceborne navigation.

Testbed	Collimated Light	Geometric Calibration	Radiometric Calibration	Stellar Objects	Non-Stellar Objects
TAS-2 ²⁵	No	No	No	Yes	No
CEL ²⁴	Yes	No	Yes	Yes	No
CRTT ²³	Yes	Yes	Yes	Yes	No
OSI ²⁶	Yes	Yes	Yes	Yes	No
OSVBS ²⁷	Yes	Yes	No	Yes	Yes

The Three-Axis Simulator 2 (TAS-2) testbed developed at the Naval Postgraduate School is a five-foot diameter simulator floating on spherical air bearings. TAS-2 was augmented with a ceiling mounted monitor to enable VBS experiments.²⁵ This monitor was positioned above a camera, with no intermediate collimating optics (CO) or radiometric verification of the visual magnitude of stars being simulated.

At the John Hopkins Applied Physics Laboratory, the Celestial Object Simulator (CEL) consists of light emitting diodes (LED) attached to an acrylic hemisphere which are used to mimic the hundred brightest singlet stars in the northern hemisphere of the night sky.²⁴ A 2-axis gimbal mechanism was used to slew the star camera positioned at the center of the hemisphere and simulate relative attitude motion. The use of individual LED allowed this group to emulate SO over 5 stellar magnitudes of dynamic range and was calibrated from a radiometric stand-point using a procedure relying on spectrometers and neutral density filters. Although the authors used a CO, they did not pursue quantifying the geometrical distortion it introduced.

Rufino and Moccia created a testing facility which consisted of a cathode ray tube monitor stimulating a ST through a CO.²³ The cathode ray tube testbed (CRTT) was enclosed in a 1.8 by 0.6 by 0.6 [m] shroud with explicit calibration efforts invested to quantify the irradiance output of the monitor versus digital count. The methodology to simulate SO was to illuminate a single pixel which limited the geometrical resolution of the testbed to the instantaneous field of view (iFOV) of a monitor pixel (~ 50 [arcsec]). The authors correct for distortions introduced by the CO in software, and quantify the temporal nature of a dynamic simulation rigorously. This testbed however did not simulate NSO within the FOV.

The Jenoptik Optical Sky field Simulator (OSI) used by the German Aerospace Center (DLR) is a compact device which is attached to an arbitrary ST through a custom adapter.²⁶ A simulated scene stimulates a ST with collimated light and accounts for optical distortions by warping the intended scene as well. The distortion of the CO is isolated from that of the VBS and is characterized using a pair of fourth-order calibration polynomials which results in the ability to render a single star to within ~ 10 [arcsec]. Pixel intensity is commanded using a Gaussian point-spread function based off star visual magnitudes. This testbed has the ability to render planetary objects (Sun, Moon, asteroids), but does not describe the ability to simulate satellites within the field of view (FOV).

The Optical Stimulator System for VBS (OSVBS) testbed created by the Technical University of Denmark (DTU) consists of a computer monitor viewed by a VBS through a CO.²⁷ The testbed is large and encased in a shroud, but no other mentions of radiometric emulation are described. Geometrically, the authors account for optical distortion by rendering a scene to the monitor which is warped using openCV.²⁸ The resulting attitude solutions differ in the single arc-second range from the intended attitude. The authors do not distinguish between distortion of the camera's optical elements and the distortion introduced by the CO. This testbed has the capability to simulate satellites within the FOV.

Limitations of previous optical testbeds consist of insufficiencies in angular accuracy, radiometric dynamic range, the ability to simulate a rapidly changing scene, accounting for geometric distortion, matching radiometric characteristics, maintaining portability and simulating multiple, mixed and transition navigation modes (i.e. inertial, far-range and close-range) simultaneously.

TESTBED REQUIREMENTS

The objective of this testbed is to stimulate space-capable optical hardware using synthetically created scenes which are highly representative of the space environment. The scenes of interest consist of SO and NSO, which impose their own independent set of functional and performance requirements on the testbed.

Stellar Objects

From a functional stand-point, the OS should produce an image realistic enough for a ST to obtain a lock and produce an inertial attitude solution based off of the observed SO. This overall goal imposes requirements on the systems ability to geometrically place a SO and simulate its radiometric characteristics. If the aforementioned requirements are met, simulated SO observed by a VBS can be identified within a star catalog. Ideally, the display for the OS should be able to simulate SO within the angular resolution and detection limit of the VBS, which for considered cameras are $10 - 20$ [arcsec] and a visual magnitude range of $2 - 7$, respectively. The relationship between visual magnitude and irradiance is given by

$$m = -2.5 \log_{10} \left(\frac{I_{so}}{I_0} \right) \quad (1)$$

where m is the visual magnitude of the star, I_0 is the reference irradiance of a visual magnitude 0 star ($I_0 = 3.1 \cdot 10^{-9}$ [Wm⁻²]), and I_{so} is the irradiance of an observed SO.

Using Equation 1, the aforementioned visual magnitude bounds correspond to an irradiance range of $5 \cdot 10^{-12}$ [Wm⁻²] $\leq I_{\text{so}} \leq 5 \cdot 10^{-10}$ [Wm⁻²]. The radiometric performance requirement associated with simulating SO imposed on the OS is to be able to radiate light over this irradiance range with a single OS monitor pixel.

Non-Stellar Objects

A NSO is defined to be a space object which is not a star. The introduction of a NSO into the rendered scene should take into account the objects' attitudes, inter-object separation, material properties, and positions relative to illuminating sources (Sun, Earth, etc.) at distances ranging from the sub-meter level to hundreds of kilometers. With this operating envelope in mind, the rendering architecture is sub-divided into two modes: far- and close-range simulations.

At large inter-spacecraft separations, the observing vehicle does not need to distinguish fine features of the target, but instead needs to accurately determine the line-of-sight (LOS) vector to the target NSO and background SO. In this mode the observed object will resemble a point source of light. The irradiance received by the observing vehicle is modeled as the light reflected off the NSO, which is given by

$$I_{\text{nso}} = a \left(\frac{\Omega}{2\pi} \right) I_{\text{solar}} = a \left(\frac{A}{2\pi r^2} \right) I_{\text{solar}} \quad (2)$$

where I_{nso} is the irradiance emitted by the NSO, Ω is the solid angle subtended by the NSO, a is the reflectance coefficient of the NSO, I_{solar} is the visible solar irradiance of 620 [Wm⁻²] at 1 astronomical unit (AU), A is the characteristic area of the NSO, and r is the inter-object separation. Note that the characteristic area of the NSO is functionally dependent on its attitude and position relative to an observer.

The NSO radiometric performance requirements imposed on the OS monitor are not only a function of characteristics of the simulated NSO (i.e. range of r , A , a), but also on the instantaneous field of view (iFOV) of the OS monitor pixels, iFOV_{os} . The number of OS monitor pixels, N , required to match this geometry is calculated using similar triangles, and is given by

$$N = \frac{\sqrt{\Omega}}{\text{iFOV}_{\text{os}}} \quad (3)$$

The irradiance which must be emitted by a single OS monitor pixel, I_{os} , is taken to be the quotient of I_{nso} and N^2 .

$$I_{\text{os}} = \frac{I_{\text{nso}}}{N^2} \quad (4)$$

Equation 4 is used to compute the NSO irradiance performance requirement imposed on an OS monitor pixel. For example, consider a NSO with $A = 2500$ [cm²], $a = 1 \cdot 10^{-3}$, over an inter-object separation ranging from 10 [m] to 100 [km], and $\text{iFOV}_{\text{os}} = 10$ [arcsec]. The NSO irradiance, subtended solid angle, and number of monitor pixels over a range of inter-object separation are tabulated below in Table 2.

These quantities are used with Equation 4 to compute an NSO peak irradiance performance requirement imposed on a single OS monitor pixel of $I_{\text{os}} = 2.3 \cdot 10^{-10}$ [W m⁻²].

Table 2: NSO solid angle and irradiance for a given inter-object separation. These quantities are used with a known $i\text{FOV}_{\text{os}}$ to compute the number of pixels required to match NSO irradiance.

r	$\sqrt{\Omega}$	I_{nsO}	N
[m]	[deg]	[Wm^{-2}]	[pixels]
$1 \cdot 10^5$	$5 \cdot 10^{-6}$	$2.5 \cdot 10^{-12}$	$1 \cdot 10^{-1}$
$1 \cdot 10^4$	$5 \cdot 10^{-5}$	$2.5 \cdot 10^{-10}$	$1 \cdot 10^0$
$1 \cdot 10^3$	$5 \cdot 10^{-4}$	$2.5 \cdot 10^{-8}$	$1 \cdot 10^1$
$1 \cdot 10^2$	$5 \cdot 10^{-3}$	$2.5 \cdot 10^{-6}$	$1 \cdot 10^2$
$1 \cdot 10^1$	$5 \cdot 10^{-2}$	$2.5 \cdot 10^{-4}$	$1 \cdot 10^3$

DESIGN SUMMARY OF OPTICAL STIMULATOR

The OS consists of an organic light-emitting diode (OLED) monitor which is commanded over a video graphics array (VGA) cable by an external workstation. This OLED monitor is attached to a three-axis translational stage which is connected to a 600 [mm] by 300 [mm] optical breadboard. Light radiated by the OLED monitor stimulates a VBS mounted to the optical breadboard with post holders through a CO. The CO is housed in a threaded mount which can translate along optical rails parallel to the optical axis of the CO. COs of different focal length can readily be interchanged to stimulate VBS with different FOV. Figure 1 depicts the computer aided design (CAD) concept of the OS. The physically realized testbed is depicted in Figure 2.

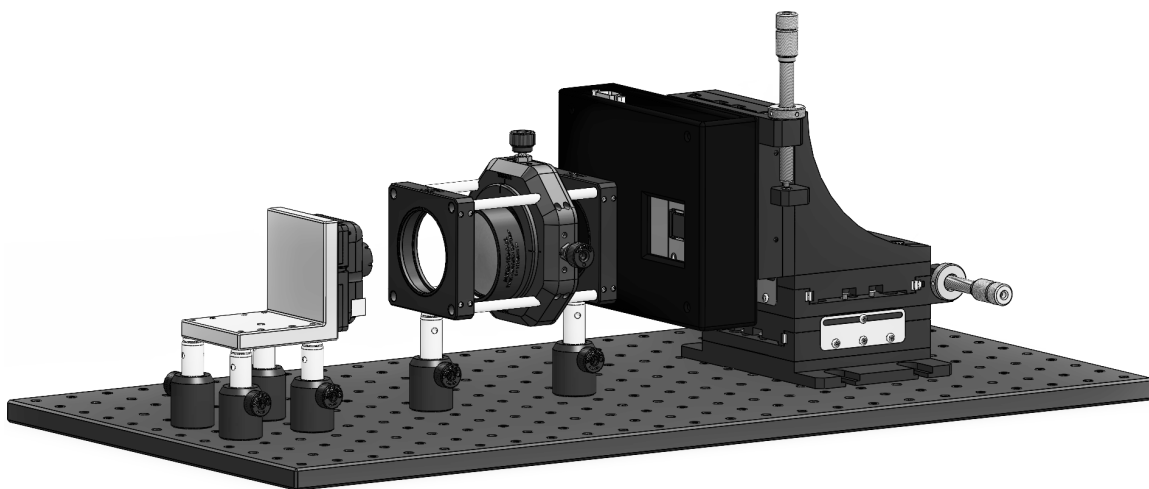


Figure 1: CAD design of the OS.

Collimating Optic Selection

The single lens configuration, depicted in Figure 3, must give the rendered image the correct size and location for a given intercomponent separation. The governing equations which must be met to achieve this impose consistency with optical separations, geometry, and magnification. Mathematically, these equations are given by

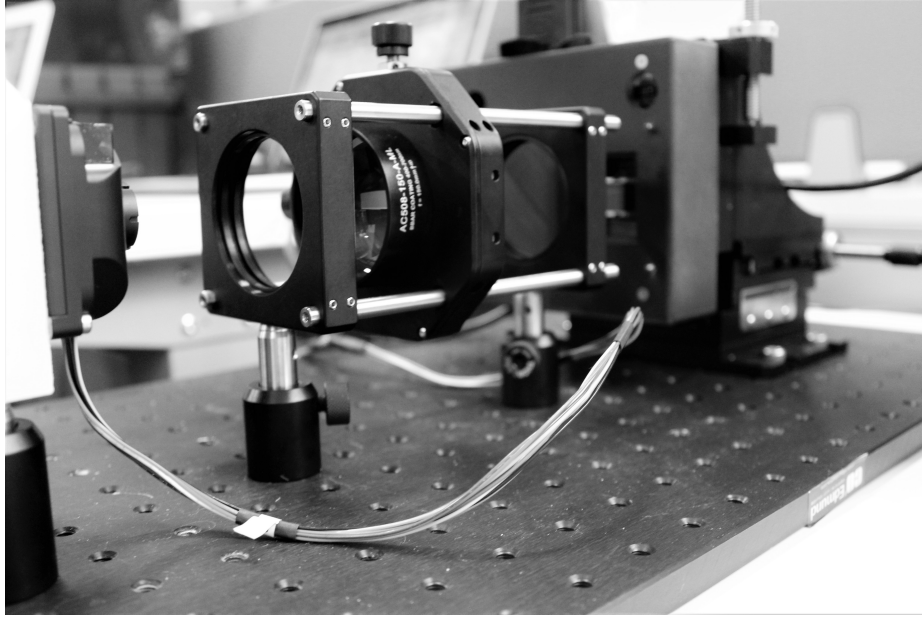


Figure 2: VBS viewing the OS monitor through CO.

$$s_i = w_d - s_{vbs} \quad (5)$$

$$x_i = 2w_d \tan\left(\frac{\theta}{2}\right) \quad (6)$$

$$\frac{1}{f_{co}} = \frac{1}{s_o} - \frac{1}{s_i} \quad (7)$$

$$x_i = x_d \frac{s_i}{s_o} \quad (8)$$

where f_{co} is the focal length of the CO, θ is the full FOV of the VBS, w_d is the working distance of the VBS, x_d, x_i are the characteristic lengths of the display/image, s_{vbs}, s_i, s_o are the separations between VBS/CO, VBS/image and CO/display respectively, and are labeled in Figure 3. All of the aforementioned parameters are assumed to be known except f_{co} and s_o , which can be solved for by combining Equations 5-8. Because the working distance of the VBS is expected to exceed the distance from the CO to the VBS by at least two orders of magnitude, the terms involving w_d cancel out and simplify to

$$s_o = \frac{x_d(w_d - s_{vbs})}{2w_d \tan\left(\frac{\theta}{2}\right)} \approx \frac{x_d}{2 \tan\left(\frac{\theta}{2}\right)} \quad (9)$$

$$f_{co} = \frac{s_o(w_d - s_{vbs})}{w_d - s_o - s_{vbs}} \approx s_o \quad (10)$$

The simplified relations are also the exact solution for when the working distance of the camera is set to infinity. The similarity between these relations illustrates that changing the working distance of the VBS introduces negligible change to the configuration when the working distance is in the range of 10 [m] to infinity. From these relations, it is clear that the focal length of the CO must be specifically selected for a given combination of VBS and display.

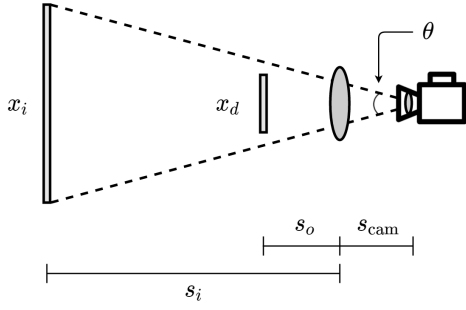


Figure 3: Single lens configuration.

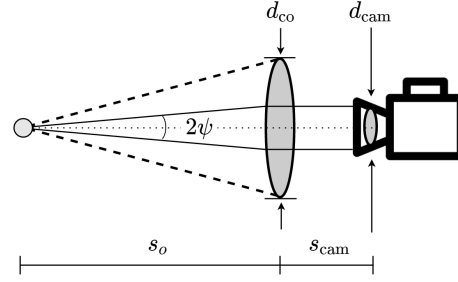


Figure 4: Single lens radiometry.

For the radiometric model of the single-lens configuration, a single monitor pixel is approximated as a Lambertian point source with maximum radiant intensity r_{pix} . The radiance of the source varies with the cosine of the angle between the observation point and the axis of the source. Note that the dispersion between the CO and the camera is effectively negligible due to the small separation and comparatively large working distance. The half-angle spanned by the optics, ψ , and power entering the camera lens, p_{cam} , are given by

$$\psi = \arctan\left(\frac{\min(d_{\text{co}}, d_{\text{vbs}})}{2s_o}\right) \quad (11)$$

$$p_{\text{vbs}} = \frac{\pi}{2} r_{\text{max}} (1 - \cos(2\psi)) = \pi r_{\text{max}} \left(\frac{1}{1 + \left(\frac{x_d}{d_{\text{vbs}} \tan(\theta/2)}\right)^2} \right) \quad (12)$$

where d_{cam} , d_{co} are the diameters of the camera and CO, respectively. The maximum power available from the pixel is achieved at $\psi = \pi/2$, corresponding to a radiance of $p_{\text{vbs}} = \pi r_{\text{max}}$. With this in mind, the power efficiency, η , of the system is given by

$$\eta = \frac{1}{1 + \left(\frac{x_d}{d_{\text{vbs}} \tan(\theta/2)}\right)^2} \quad (13)$$

Observe that the radiometric efficiency depends on the required separation between the display/CO and the diameter of the camera optic. By repeating this analysis for a dual-lens configuration, it can be shown that the radiometric efficiency is the same for the single and dual-lens configurations. The only benefit provided by the dual lens system is the ability to use a single set of lenses to accommodate a range of FOV values, at a cost of increased design complexity and calibration time.

Monitor Irradiance

As discussed in the requirements section, the OS should emulate the radiometric intensities of SO and NSO. Table 3 summarizes the lower and upper irradiance bounds required to simulate SO and NSO posed by future autonomous rendezvous missions.^{4,6,18}

Table 3: Irradiance requirements to simulate SO and NSO.

	Min Irradiance [Wm ⁻²]	Max Irradiance [Wm ⁻²]
SO	$5 \cdot 10^{-12}$	$5 \cdot 10^{-10}$
NSO	$2 \cdot 10^{-11}$	$2 \cdot 10^{-04}$

The display dynamic range should be as large as possible in order to accurately simulate dim SO and bright NSO at close proximity. A market survey identified that most COTS monitors have individual pixels which span 2-3 orders of radiometric magnitude. By allocating a large number of adjacent monitor pixels, the radiometric output of the monitor can span several orders of magnitude. For example, a monitor with $2 \cdot 10^6$ [pixels] and single pixel irradiance of 10^{-8} [Wm^{-2}] is capable of matching irradiance levels up to $2 \cdot 10^{-2}$ [Wm^{-2}]. By selecting a monitor with over $2 \cdot 10^6$ [pixels] and a individual pixel dynamic range of 10^{-11} through 10^{-8} [Wm^{-2}] all SO and NSO of interest (with respect to the testbed requirements) can be simulated.

CALIBRATION OF OPTICAL STIMULATOR

After completion of the mechanical design of the OS, the testbed needs to be calibrated to simulate SO and NSO. The calibration is necessary to geometrically place accurate radiometric point sources of light within the VBS FOV in the presence of optical distortions introduced by the CO. The overall calibration is composed of a geometric and radiometric calibration.

Geometric Calibration

A VBS referred to as the calibration article is independently calibrated using techniques outlined by Beierle et al.²⁹. After calibration, this VBS is capable of reporting undistorted unit vectors to features observed in the FOV. The calibration article is then stimulated by an orthogonal grid of dots rendered to the OS monitor. The mounting of the calibration article with respect to the OS can be calculated using q-method.³⁰ With an estimated mounting, undistorted unit vectors to observed calibration features can be computed by the calibration article. These unit vectors will deviate from the expected angular location coming from a pinhole model due to the intrinsic parameters of the CO. These deviations allow for the estimation of distortion coefficients which characterize the CO. Further details of this procedure are available in the work of Beierle et al.²⁹

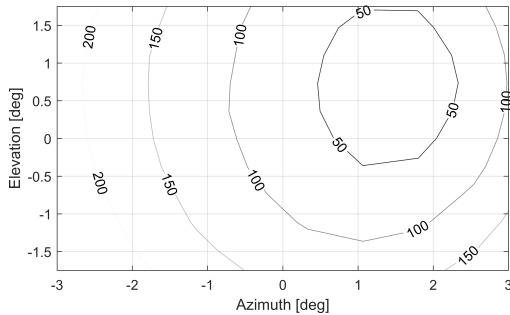


Figure 5: Starting point of the CO calibration. Contours represent angular residuals between the intended and observed angular location being simulated. These contours have units of arcseconds.

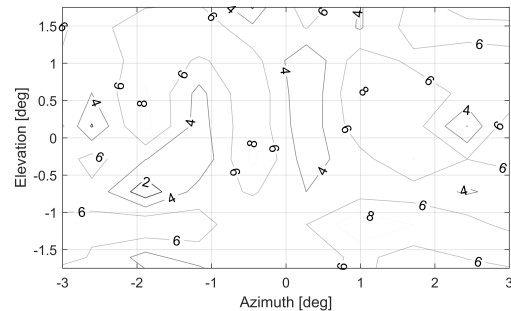


Figure 6: Final point of the CO calibration. Contours represent angular residuals between the intended and observed angular location being simulated. These contours have units of arcseconds.

The geometrical impact of the CO calibration procedure is shown in Figures 5 and 6. The contours of these plots represent the angular differences in arcseconds between the reference set of monitor calibration features and the observed calibration article features before and after calibrating for the CO. The quality of the CO calibration is quantified through the magnitude of the residuals depicted in Figure 6, which are fundamentally related to the iFOV of the VBS calibration article. The angular range of residuals in Figure 6 correspond to 5% –30% of the iFOV associated with a calibration article pixel.

Radiometric Calibration

The irradiance emitted by the OS monitor was measured using an optical power meter placed at the exit of the CO. Measurements were obtained by illuminating a square block of N^2 pixels on the OS monitor and varying the digital count of the block from 0 to 255. The total irradiance measurements were then normalized by N^2 to compute the average irradiance output of a single OS monitor pixel as a function of monitor digital count. These results are plotted in Figures 7 and 8. These results demonstrate the ability to simulate sources of light near $1 \cdot 10^{-12}$ [Wm^{-2}] all the way up to $1 \cdot 10^{-4}$ [Wm^{-2}], which corresponds to a radiometric dynamic range spanning eight orders of magnitude.

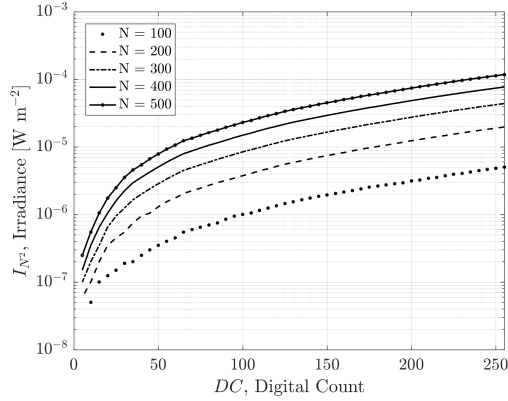


Figure 7: Total irradiance measured at the exit of CO plotted against OS monitor digital count.

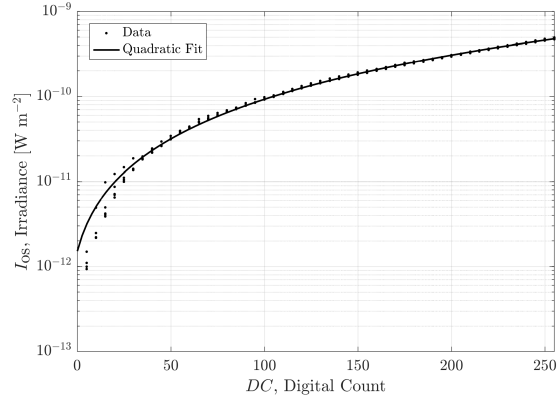


Figure 8: Average irradiance of a single OS monitor pixel measured at the exit of CO plotted against digital count.

The outputs of the OS geometric and radiometric calibration are distortion coefficients characterizing the CO, the extrinsic parameters encoding the alignment between the VBS and the OS, and an empirical mapping from monitor digital count to irradiance exiting the CO.

VALIDATION OF OPTICAL STIMULATOR

Once the OS has been calibrated, the testbed has the ability to simulate precise radiometric point sources of collimated light at an intended angular location. Prior to utilizing the OS for the characterization of VBS, a set of validation analyses are performed to affirm functionality and the quality of the previous calibration steps.

Geometric Validation

Functional and performance validation of the OS geometric calibration was performed with two separate tests. The functional test utilized flight data from the ARGON experiment to affirm that the OS qualitatively is placing SO and NSO at the correct geometric locations. ARGON flight data consisted of images taken by the Mango far-range VBS, precise orbit determination (POD) products accurate to the centimeter level in relative position, and an inertial navigation solution coming from star trackers.^{1,31} The software used to synthesize images for the OS computed the geometric location of SO and NSO with the aforementioned inputs. The angular location of SO and NSO computed by the OS was then projected and super-imposed onto the corresponding ARGON flight image depicted in Figure 9.

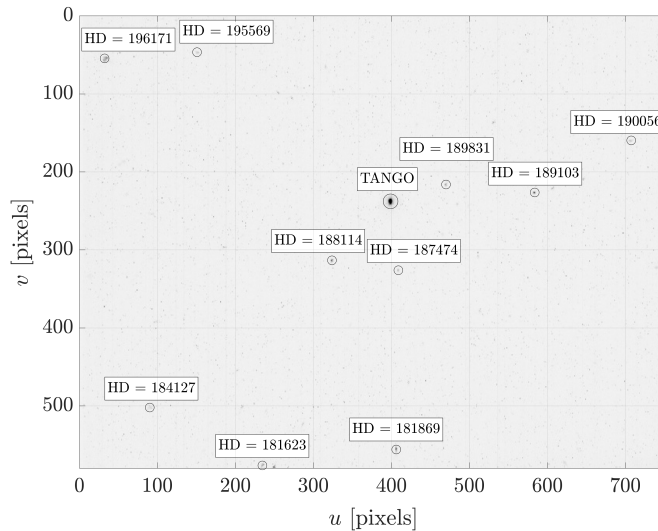


Figure 9: ARGON flight image from PRISMA mission of Tango acquired by Mango far-range VBS at 14 [km] separation on 2012-04-25.¹ The geometric location of SO calculated by the OS are super-imposed over the flight image and annotated with Henry Draper (HD) identifiers. POD flight products are used by the OS to calculate the geometric centroid of the NSO. Functionally, both SO and NSO predicted by the OS match up with the PRISMA flight data and imagery.

The alignment of synthetic OS features with SO and NSO in the ARGON flight image indicate that the OS is functionally able to render SO and NSO with geometric consistency, but it does not indicate the accuracy to which these features can geometrically be placed. For this purpose, a separate performance validation is developed to quantify the geometric accuracy of the OS. The performance validation test renders a warped grid of dots to the OS monitor which stimulates the calibration article. For each of the features observed by the calibration article, an angular residual, $d\theta$, is computed as

$$d\theta = \cos^{-1} \left(\hat{\mathbf{n}}_{\text{des}}^T \hat{\mathbf{n}}_{\text{meas}} \right) \quad (14)$$

where $\hat{\mathbf{n}}_{\text{meas}}$, $\hat{\mathbf{n}}_{\text{des}}$ are the desired and measured feature unit vectors, respectively. These angular residuals were computed for each dot. Statistics associated with the angular residuals are summarized in Table 4, and a plot of the angular residuals cumulative distribution function (CDF) is depicted in Figure 10. These results indicate that point sources of light are stimulating the VBS from the intended angular location (in the presences of CO distortions) at levels of accuracy which are less than a fraction of a calibration article pixel.

Table 4: Statistics on angular residuals, $d\theta$, from the OS geometric verification. The mean and standard deviation of the experimentally computed angular residuals are given by $\overline{d\theta}$ and σ , respectively. All units are in [arcsec]

$\overline{d\theta}$	1σ	3σ
5.0878	2.9422	8.8265

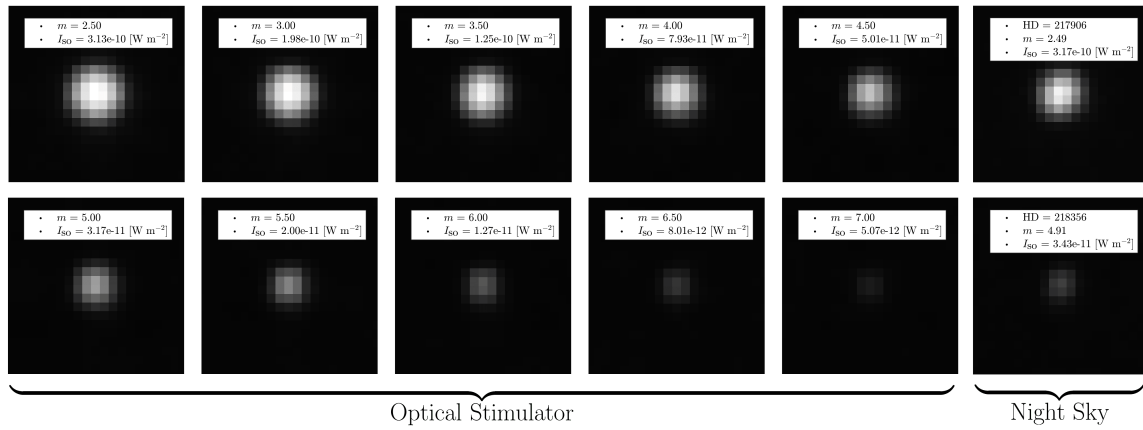


Figure 11: Images acquired by calibration article being stimulated by OS monitor and night sky.

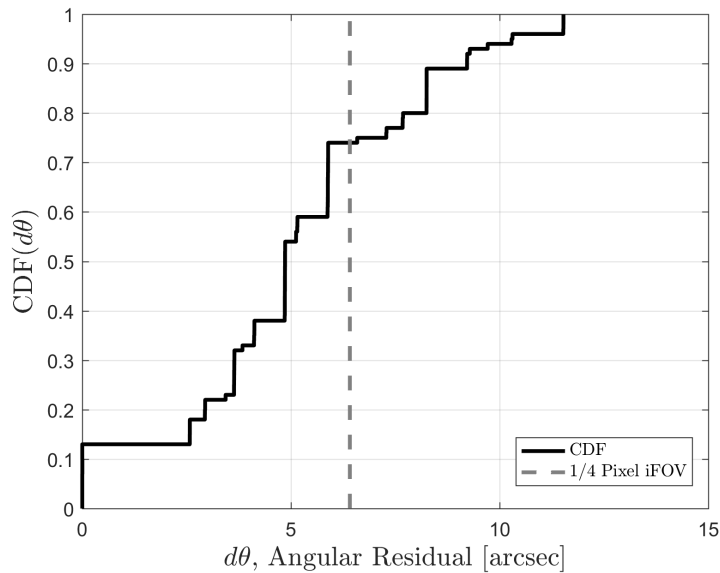


Figure 10: Cumulative distribution function of the angular residual, $d\theta$, between the measured and intended geometric location of verification features observed by the calibration article. A vertical line representing the 25% of the instantaneous field of view (iFOV) of a pixel on the calibration article detector is plotted for reference.

Radiometric Validation

Validation of the radiometric calibration of the OS was performed using the images of the night sky collected by the calibration article. SO observed by the calibration article were identified and used to infer the source irradiance with Equation 1. This irradiance was then used to command the OS monitor which in turn stimulated the same calibration article. The two sets of images are depicted in Figure 11.

Equation 1 however does not account for any attenuation of the source irradiance as light propagates through the atmosphere of our planet. This un-modeled characteristic is hypothesized to be the predominant factor producing differences in detector responses between observations of SO from the OS and night sky. The radiometric characteristics of the images in Figure 11 are tabulated in Table 5. A 50% attenuation value

is tabulated in Table 5 for reference.

Table 5: Radiometric quantities from night sky collect compared to OS observations.

	Optical Stimulator					Night Sky	
	Observed					Observed	50% Atten.
	m	2.5	3.0	3.5	4.0	4.5	2.49
I_{so} [Wm^{-2}]	3.13e-10	1.98e-10	1.25e-10	7.93e-11	5.01e-11	3.16e-10	1.58e-10
$\sum DC$	2271904	2033248	1773088	1560928	1333104	1707296	-
m	5.0	5.5	6.0	6.5	7.0	4.91	5.67
I_{so} [Wm^{-2}]	3.17e-11	2.00e-11	1.27e-11	8.01e-12	5.07e-12	3.44e-11	1.72e-11
$\sum DC$	1146704	999872	831904	742960	670112	924352	-

RESULTS

With a calibrated and validated OS, the testbed is ready to simulate both static and dynamic scenarios consisting of SO and NSO using the rendering architecture presented in the work by Beierle et al.²⁹

Inertial Navigation Simulation

A moving star field was rendered to the OS monitor and used to stimulate a VBS test article undergoing a constant angular velocity slew relative to an Earth-centered inertial reference frame (ECI). For low enough angular velocities, the VBS test article immediately returned a lock corresponding to the simulated star field with an angular offset. This angular offset was encoded with a direction cosine matrix (DCM) given by

$$\mathbf{R}_{gt}^{meas} = \mathbf{R}_{eci}^{meas} (\mathbf{R}_{eci}^{gt})^T \quad (15)$$

where \mathbf{R}_{eci}^{gt} is the ground truth OS simulated vehicle attitude with respect to ECI, \mathbf{R}_{eci}^{meas} is the vehicle attitude with respect to ECI measured by the ST, and \mathbf{R}_{gt}^{meas} is the ST measured attitude with respect to the OS simulated attitude. If the two former attitudes are identical, then \mathbf{R}_{gt}^{meas} will be identity.

Images corresponding to this scenario definition were created a-priori and then rendered to the OS monitor in an open-loop fashion through Simulink with custom written s-functions. The refresh rate of the OS monitor is listed to be within 30 – 85 [Hz] which corresponds to a duration between sequential updates in the range of 12.5 – 33.3 [ms]. With this duration in mind, the ground-truth time-step between sequential synthetic images was selected to be 50 [ms]. To ensure the a-priori produced images were rendered at the intended time, an s-function was written to perform time synchronization with the Simulink simulation and the clock of the host workstation. This time synchronization block consists of a conditional while loop preventing execution of downstream code. The condition to exit the while loop is for a configurable amount of time to have passed, which is determined by a query to the internal oscillator of the host workstation. Additional s-function blocks within the simulation interface with the VBS test article and trigger image acquisitions. The interface to OS monitor and VBS along with the software to synchronize Simulink with the workstation clock all exist within a single simulation. This allows the timestamp of the acquired images to be compared directly to the ground-truth for assessing VBS solution quality and functional capabilities as a function of the inertial angular velocity of the sensor.

A series of three inertial dynamic experiments were conducted with different ground truth angular velocities. Unit vector measurements were derived from the HIL acquired images. Equation 14 was used to compute angular residuals between the measured and ground truth unit vectors over the duration of the experiment. The interior angle associated with these inner-products is on the order of tens of arcseconds for the three conducted experiments, and is depicted in the cumulative distribution function (CDF) in Figure 13.

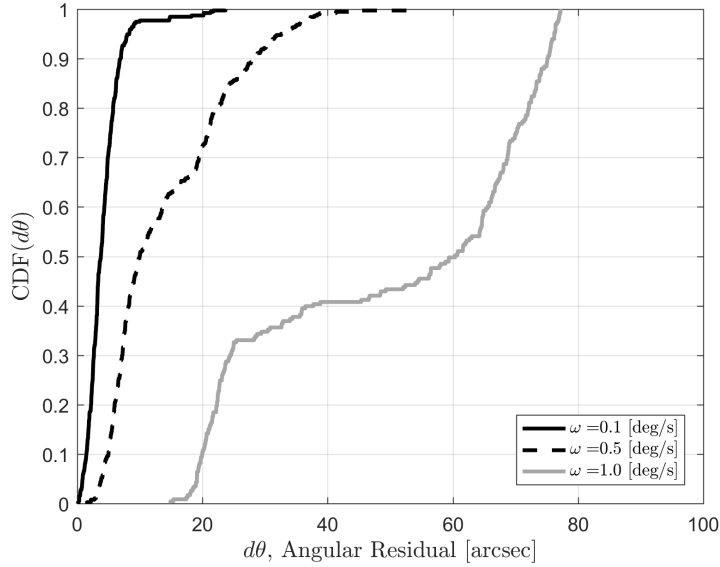


Figure 13: Cumulative distribution function of angular residuals computed for dynamic inertial navigation simulation.

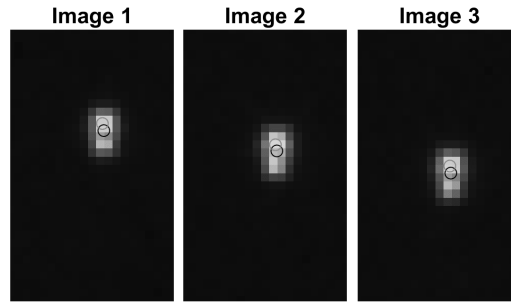


Figure 12: HIL acquired images from the inertial dynamic simulation with 0.5 [deg/s] angular velocity slew.

The CDF plotted in Figure 13 reveals many interesting facets about the VBS test article. Observe that simulations corresponding to lower ground truth angular velocities have smaller angular residuals for all values of the CDF function. The CDF corresponding to the low angular velocity simulations has a smoothly varying nature, which is hypothesized to be a result of the image processing algorithm behaving more reliably with a slowly varying angular location of the integrated point source of light. As the angular velocity of the inertial dynamic simulation increases, the VBS test article observes stars with larger streaks, as seen in Figure 12. As the signal to noise ratio of these streaking stars decreases, the quality of the image processing algorithm correspondingly degrades. The manifestation and quantification of this phenomenon is all encoded in Figure 13. The ability to simulate these scenarios on the ground has enormous potential to facilitate procedural decisions for commissioning of spacecraft, safe-modes, and nominal dynamic operations.

Relative Navigation Simulation

The final test scenario considered in this work looks at the problem of dynamic relative navigation of the observing spacecraft with respect to a NSO in near-circular, low Earth orbit (LEO). In this configuration, the observer spacecraft is attempting to estimate the relative orbital motion of the target space object using only bearing angles obtained by the VBS. This so-called angles-only navigation has been considered in several

research studies,⁷⁻¹³ and utilized for relative navigation and rendezvous in both the ARGON experiment,¹ as well as the Autonomous Vision Approach Navigation and Target Identification (AVANTI) experiment³² taking place during the Firebird mission (DLR). Angles-only relative navigation represents an especially difficult estimation scenario due to the inherent dynamical observability constraints imposed by using bearing angle measurements (2D) to reconstruct the full relative orbital motion state (6D). The stability and performance of algorithms developed for angles-only navigation can be verified with greater confidence using the OS since it introduces a higher degree of realism in the verification process (i.e., the use of a real sensor in the loop) than pure software simulation methods.

For this paper, the NSO relative orbital motion is chosen to recreate one of the scenarios considered by Sullivan et al.¹¹ in the context of angles-only rendezvous in LEO. In that work, the authors use a set of relative orbital elements (ROE) consisting of the relative semi-major axis (δa), the relative mean longitude ($\delta \lambda$), and the relative eccentricity and inclination vectors (δe and δi) to parameterize the relative motion of the NSO with respect to the observing spacecraft.³³ The initial conditions for the observing spacecraft and the relative motion of the NSO are provided in Table 6.

Table 6: Initial servicer orbital conditions and mean ROE test case for dynamic simulation.¹¹

Servicer Orbit	$a = 7200$ [km]	$e = 0.001$	$i = 30^\circ$	$\Omega = 60^\circ$	$\omega = 120^\circ$	$M_0 = 0^\circ$
Initial ROE	$a\delta a$ [m]	$a\delta \lambda$ [m]	$a\delta e_x$ [m]	$a\delta e_y$ [m]	$a\delta i_x$ [m]	$a\delta i_y$ [m]
ROE 2	-100	-20,000	300	0	-300	0

Note that these initial ROE correspond to relative motion that begins with a mean along-track separation of -20 [km], a projected circular motion with 300 [m] amplitude in the NR-plane, and a relative drift of approximately 1 [km] per orbit in the along-track direction induced by a nonzero relative semi-major axis. For simplicity but without loss of generality, the VBS on the observing spacecraft is assumed to be mounted with a fixed boresight alignment in the anti-flight direction. Under this assumption, the relative position vectors in the VBS, $\{{}^{\text{vbs}}\rho$, and RTN frames, $\{{}^{\text{rtn}}\rho$, are related by

$$\{{}^{\text{vbs}}\rho = \mathbf{R}_{\text{rtn}}^{\text{vbs}} \{{}^{\text{rtn}}\rho = \begin{bmatrix} 1 & 0 & 0 \\ 0 & 0 & 1 \\ 0 & -1 & 0 \end{bmatrix} \{{}^{\text{rtn}}\rho \quad (16)$$

where $\mathbf{R}_{\text{rtn}}^{\text{vbs}}$ is the DCM between the RTN and VBS frames.

Beginning from the specified initial conditions, the absolute position and velocity of the observing spacecraft and target NSO are numerically propagated for several orbits using a high-fidelity simulator which includes rigorous force models of high-order gravity, atmospheric drag, solar radiation pressure, third body Sun and Moon effects, and tidal effects.³⁴ The numerically propagated trajectories provide the ground truth against which to compare the performance of angles-only navigation filter. In order to estimate the relative orbit of the NSO, the filter requires knowledge of both the observer's absolute position and velocity and VBS-frame absolute attitude, as well as sequential sets of bearing angles which subtend the LOS vector pointing from the observer to the NSO. The observer absolute orbit knowledge is provided by corrupting the ground truth observer orbit with measurement noise that is representative of coarse Position/Velocity/Time (PVT) solutions obtained using a GPS receiver. Instead, the sensor in the OS testbed loop provides the measured attitude and bearing angles.

The ground truth orbit and attitude of the observer and target are provided to the OS at each time-step in order to render the NSO and a collection of SO on the testbed monitor. Additionally, the target NSO is modeled as a 1U cubesat of side length 10 [cm], with homogeneous planar panels of an assumed reflectance coefficient $a = 0.2$. In accordance with the architecture presented in the work of Beierle et al.,²⁹ all trajectory, attitude, and NSO parameters are used to calculate the scene geometry and radiometry, which are then mapped to the OS monitor. A series of hardware-in-the-loop (HIL) VBS measurements are acquired by the test article using the realistic and dynamic rendering of the NSO and SO from the OS. From these measurements, the VBS-frame absolute attitude is computed in the same manner as described in inertial navigation section

The bearing angles can be obtained by centroiding the NSO pixel cluster with a digital count weighted average. Note that the ground truth bearing angles, denoted as the azimuth (α_{truth}) and elevation (ϵ_{truth}), can be expressed directly as functions of the VBS frame rectilinear relative position vector, as given by

$$\alpha_{\text{truth}} = \arcsin\left(\frac{\{\text{vbs}\} \rho_y}{\|\boldsymbol{\rho}\|}\right) \quad (17)$$

$$\epsilon_{\text{truth}} = \arctan\left(\frac{\{\text{vbs}\} \rho_x}{\{\text{vbs}\} \rho_z}\right) \quad (18)$$

The relationship between the bearing angles and the relative position is illustrated in Figure 14.

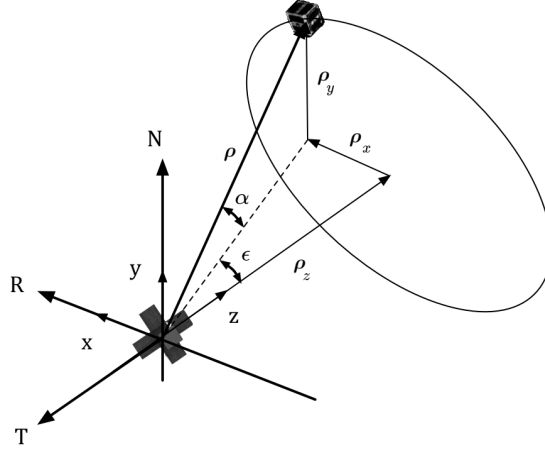


Figure 14: Relationship between relative position and bearing angles.¹¹

A simplified architectural layout of the angles-only relative navigation algorithm is depicted in Figure 15. Regions of interest (ROI) obtained from the VBS are fed into an image processing algorithm to detect and link clusters of bright pixels. Utilizing the Hipparcos star catalog, a star identification process labels some of these clusters as SO and produces an inertial attitude estimate, q . The remaining bright clusters are taken to be NSO candidates. Prior information on the orbital elements, $\vec{o}\vec{e}$, of the servicer and target NSO are assumed to be available. This absolute orbit knowledge aides in the selection of the NSO candidate to be navigated relative to. A line-of-sight vector to the NSO is used to compute bearing measurements, α, ϵ , which are fed into an adaptive unscented Kalman filter (A-UKF) formulated by Sullivan and D'Amico.^{12,13} The A-UKF returns an estimate of relative orbital elements, $\delta\vec{o}\vec{e}$, to the NSO and covariance matrix, \mathbf{P} .

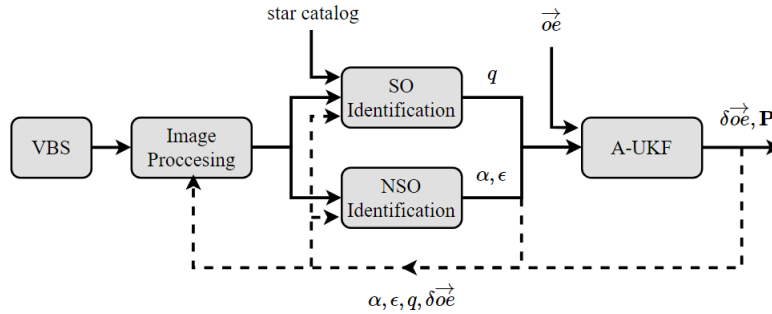


Figure 15: Simplified architecture of angles-only relative navigation algorithm. Dotted lines indicate feedback signals which aide in future execution of processes.

The differences between the ground truth bearing angles and bearings angles measured by test article are plotted in Figure 16, and their mean and standard deviation over the last three simulated orbits are tabulated in Table 7 (first row). The magnitude of these angular residuals is highly dependent on the angular resolution of the VBS test article, the quality of the OS geometric calibration, and the amount of pixel saturation resulting from modeling the NSO as a multi-variate Gaussian. It is important to note that the worst-case test article azimuth and elevation residuals in Table 7 corresponds to angular errors of less than a quarter of the pixel iFOV (34.2 [arcsec]).

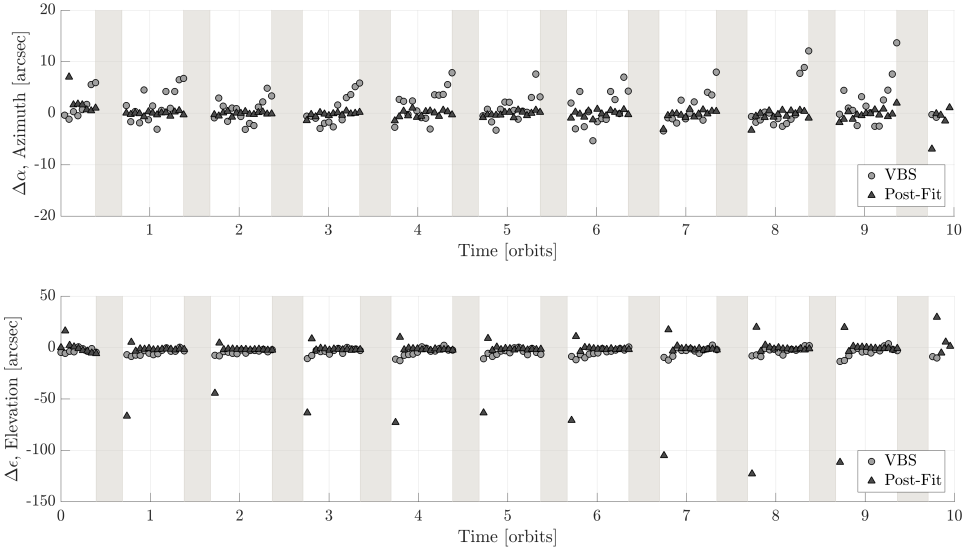


Figure 16: Differences between ground truth and VBS measured bearing angles from OS HIL dynamic relative simulation of the NSO are plotted on the left. Pre-fit and post-fit measurement residuals from adaptive unscented Kalman filter are plotted on the right. The vertical gray bars represent periods of eclipse.

The pre- and post-fit measurement residuals (i.e., the difference between the obtained measurement and modeled measurements computed before and after the Kalman filter measurement update) and ROE estimation errors with $1\text{-}\sigma$ formal standard deviations are shown in Figures 16 and 17, respectively. These results are obtained by providing an A-UKF with the HIL-acquired measurements of the observer attitude and the NSO bearing angles.

A comparison of the angles-only filter pre-fit and post-fit measurement residual steady-state statistics in Table 7 indicate worst-case post-fit residuals for azimuth and elevation at approximately 8% and 22% of the iFOV associated with a test article pixel, respectively. It is instructive to mention that the larger standard deviation in the elevation angle post-fit residuals is expected, since the range ambiguity translates to an elevation error in filter modeling due to the orbit curvature. The filter post-fit trends in Figure 16 indicate large transient residuals in the modeled measurements (particularly for the elevation angle) directly following eclipse periods. Again, this is expected since the modeled azimuth angles following eclipse are conditioned on a state estimate that has been propagated through the entire eclipse without conducting a single measurement update. Still, the subsequent steady-state post-fit elevation residuals account for worst-case angular errors that are less than a quarter of the pixel iFOV. This is a strong indication that the filter is processing measurements effectively and reducing modeling residuals to the noise floor of the onboard sensor.

Similarly, the filter is clearly able to converge to a very good estimate of the relative orbit of the NSO, demonstrating steady-state ROE estimation errors within 1% of their respective ground truth values (see Figure 17). This HIL implementation of angles-only navigation demonstrates the utility of the OS testbed for calibration and verification of VBS and algorithms across a wide swath of the radiometric and geometric

operational spectrum.

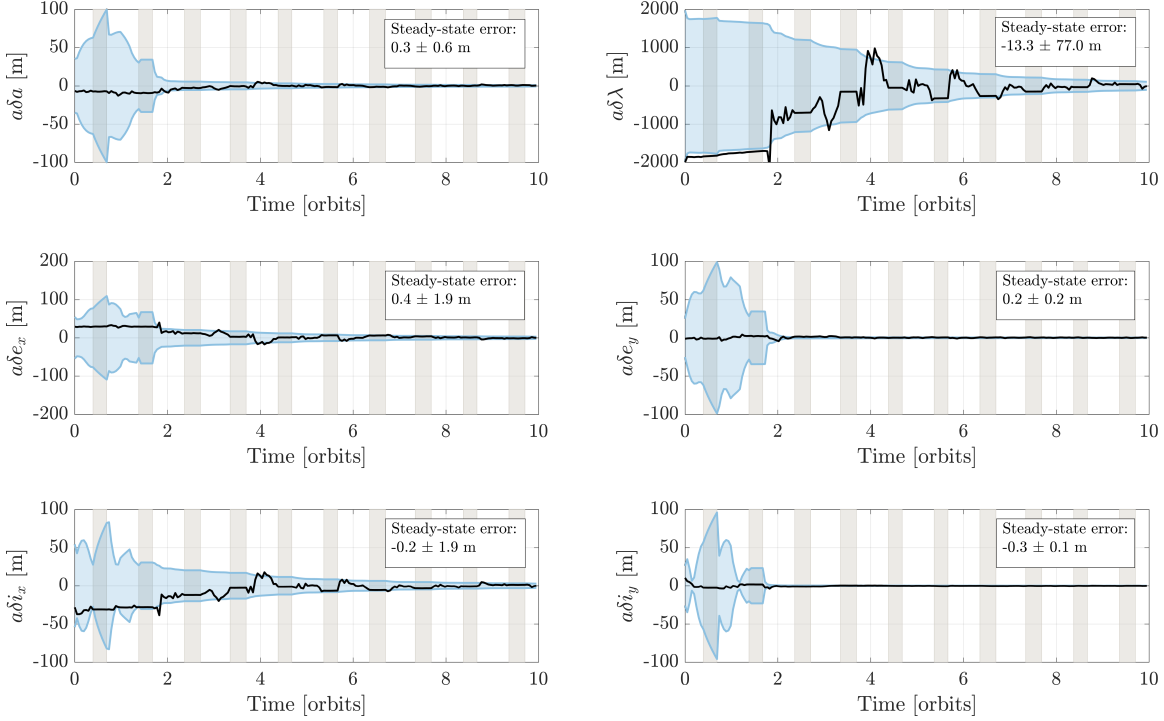


Figure 17: ROE estimation errors from the adaptive unscented Kalman filter. Vertical gray bars represent periods of eclipse.

Table 7: Statistics of the VBS and filter residuals for the dynamic relative navigation simulation over the last three simulated orbits. The azimuth and elevation residual means, $\overline{\Delta\alpha}$, $\overline{\Delta\epsilon}$, and 1σ standard deviations are reported in units of [arcsec].

	$\overline{\Delta\alpha} \pm 1\sigma$	$\overline{\Delta\epsilon} \pm 1\sigma$
VBS	$+1.62 \pm 04.09$	-3.56 ± 03.92
Pre-Fit	-2.58 ± 36.76	-5.18 ± 58.22
Post-Fit	-0.89 ± 1.77	$+1.03 \pm 07.00$

CONCLUSIONS

This paper addresses the design, calibration, validation and utilization of a HIL testbed to simulate optical hardware for spaceborne vision-based navigation. The assembled testbed and selected components were converged upon through a design process to meet an explicit set of functional and performance requirements to simulate SO and NSO from a geometric and radiometric stand-point. The OS consists of an OLED monitor stimulating a VBS through a CO. A variety of mechanical decisions were made to facilitate the realization of inter-component separation, alignment, orientation and interchangeability. Geometric calibration of the testbed consisted of isolating the distortions introduced by the CO and warping the scene rendered to the monitor to yield a collimated beam of light reaching the aperture of the VBS test article to be stimulated. A radiometric calibration quantified the irradiance of an OS monitor pixel as a function of digital count. These calibration steps were necessary to be able to accurately place simulated sources of light to within tens of arcseconds of angular accuracy over a large radiometric dynamic range. The quality of the geometric and radiometric calibrations were then validated both geometrically and radiometrically. The geometric valida-

tion consisted of a functional comparison against PRISMA flight data and imagery, while the performance validation demonstrated angular residuals between intended and measured point sources of light on the order of tens of arcseconds. The radiometric validation compared experimental results obtained from stimulating a calibration article with the OS against an independent set of measurements acquired from images of the real night-sky.

A series of experiments were conducted to stimulate a VBS test article with high-fidelity synthetic scenes which emulate the space environment. The first test simulated a moving star-field used for inertial navigation. Functional capability of the VBS test article was verified having returned a consistent inertial attitude solution corresponding to the simulated star field. The synthetically created images were rendered to the OS monitor in an open-loop, temporally regulated fashion via custom written s-functions utilized in the Simulink environment. Results from the HIL acquired imagery provided the ability to characterize the performance of a ST in terms of functionality and performance over varying levels of simulated angular velocities. A rendezvous HIL simulation was then conducted to verify the functionality and performance of a new optical angles-only navigation article. The relative navigation algorithm uses VBS measurements collected by a servicer spacecraft performing far-range rendezvous with a noncooperative client in LEO. These HIL observations were used to produce a sequence of inertial attitude measurements as well as bearing measurements to the NSO, whose relative position is unknown to the observing vehicle. This vision-based rendezvous scenario has a documented unobservability in discerning the relative separation which can be circumvented through the use of an angles-only filter. The high-dynamic range OS was able to accurately reproduce both SO and NSO from a geometric and radiometric standpoint simultaneously to stimulate the VBS test article in a realistic manner. The angles-only relative navigation algorithm was verified by assessing functional performance of the estimation solution and filter measurement modeling accuracy. Future work includes extending the capability of the OS to synthesize and render images in closed-loop and real-time as well as handle close-proximity scenes.

REFERENCES

- [1] S. D'Amico, J.-S. Ardaens, G. Gaias, H. Benninghoff, B. Schlepp, and J. L. Jørgensen, "Noncooperative Rendezvous Using Angles-Only Optical Navigation: System Design and Flight Results," *Journal of Guidance, Control, and Dynamics*, Vol. 36, Nov. 2013, pp. 1576–1595, 10.2514/1.59236.
- [2] S. D'Amico, J.-S. Ardaens, G. Gaias, B. Schlepp, H. Benninghoff, T. Tzschichholz, T. Karlsson, and J. L. Jørgensen, "Flight Demonstration of Non-Cooperative Rendezvous using Optical Navigation," *23th International Symposium on Space Flight Dynamics*, Pasadena, CA, USA, Oct. 2012.
- [3] J. Christian, M. Patangan, H. Hinkel, K. Chevray, and J. Brazzel, "Comparison of Orion Vision Navigation Sensor Performance from STS-134 and the Space Operations Simulation Center," *American Institute of Aeronautics and Astronautics*, Aug. 2012, 10.2514/6.2012-5035.
- [4] J. Kolmas, P. Banazadeh, A. W. Koenig, S. D'Amico, and B. Macintosh, "System Design of a Miniaturized Distributed Occulter/Telescope for Direct Imaging of Star Vicinity," *Yellowstone Conference Center, Big Sky, Montana*, Mar. 2016.
- [5] S. Seager, W. Cash, S. Domagal-Goldman, N. J. Kasdin, M. Kuchner, A. Roberge, S. Shaklan, W. Sparks, M. Thomson, M. Turnbull, K. Warfield, D. Lisman, R. Baran, R. Bauman, E. Cady, C. Heneghan, S. Martin, D. Scharf, R. Trabert, D. Webb, and P. Zarifian, "Exo-S: Starshade Probe-Class Exoplanet Direct Imaging Mission Concept Final Report," final Report, NASA, Jet Propulsion Laboratory, Mar. 2015.
- [6] C. W. Roscoe, J. J. Westphal, S. Lutz, and T. Bennett, "Guidance, Navigation, and Control Algorithms for Cubesat Formation Flying," *38th AAS Guidance and Control Conference*, Breckenridge, CO, AAS, Jan. 2015.
- [7] D. C. Woffinden and D. K. Geller, "Relative Angles-Only Navigation and Pose Estimation for Autonomous Orbital Rendezvous," *Journal of Guidance, Control, and Dynamics*, Vol. 30, No. 5, 2007, pp. 1455–1469.
- [8] D. C. Woffinden and D. K. Geller, "Observability Criteria for Angles-Only Navigation," *IEEE Transactions on Aerospace and Electronic Systems*, Vol. 45, No. 3, 2009, pp. 1194–1208.
- [9] G. Gaias, S. D'Amico, and J.-S. Ardaens, "Angles-Only Navigation to a Noncooperative Satellite Using Relative Orbital Elements," *Journal of Guidance, Control, and Dynamics*, Vol. 37, No. 2, 2014, pp. 439–451, 10.2514/1.61494.
- [10] J.-S. Ardaens and G. Gaias, "Spaceborne Autonomous Vision-Based Navigation System for AVANTI," *Proceedings of the 65th International Astronautical Congress*, Toronto, Canada, 2014.

- [11] J. Sullivan, A. Koenig, and S. D’Amico, “Improved Maneuver-Free Approach to Angles-Only Navigation for Space Rendezvous,” *26th AAS/AIAA Space Flight Mechanics Meeting, Napa, CA*, Feb. 2016.
- [12] J. Sullivan and S. D’Amico, “Adaptive Filtering for Maneuver-Free Angles-Only Navigation in Eccentric Orbits,” *27th AAS/AIAA Space Flight Mechanics Conference*, San Antonio, Texas, 2017.
- [13] J. Sullivan and S. D’Amico, “Nonlinear Kalman Filtering for Improved Angles-Only Navigation Using Relative Orbital Elements,” *Journal of Guidance, Control and Dynamics*, 2017. Accepted.
- [14] M. Leinz, C.-T. Chen, M. W. Beaven, T. P. Weismuller, D. L. Caballero, W. B. Gaumer, P. W. Sabastean-ski, P. A. Scott, and M. A. Lundgren, “Orbital Express Autonomous Rendezvous and Capture Sensor System (ARCSS) flight test results,” *Proceedings of SPIE*, Vol. 6958, 2008, pp. 69580A–69580A–13, 10.1117/12.779595.
- [15] A. Petit, E. Marchand, and K. Kanani, “Vision-based space autonomous rendezvous: A case study,” 2011, pp. 619–624, 10.1109/IROS.2011.6048176.
- [16] S. D’Amico, M. Benn, and J. L. Jørgensen, “Pose Estimation of an Uncooperative Spacecraft from Actual Space Imagery,” *International Journal of Space Science and Engineering*, Vol. 2, No. 2, 2014, p. 171, 10.1504/IJSPACESE.2014.060600.
- [17] S. Sharma and S. D’Amico, “Reduced-Dynamics Pose Estimation for Non-Cooperative Spacecraft Rendezvous using Monocular Vision,” *38th AAS Guidance and Control Conference*, Breckenridge, Colorado, 2017.
- [18] B. B. Reed, R. C. Smith, B. J. Naasz, J. F. Pellegrino, and C. E. Bacon, “The Restore-L Servicing Mission,” *AIAA SPACE 2016*, p. 5478, AIAA, 2016, 10.1109/ICCV.1999.791289.
- [19] D. L. Wenberg, B. P. Keegan, M. E. Lange, E. A. Hanlon, and J. S. Kang, “RSat Flight Qualification and Test Results for Manipulable Robotic Appendages Installed on 3U CubeSat Platform,” 2016.
- [20] N. Strange, D. Landau, T. McElrath, G. Lantoine, and T. Lam, “Overview of Mission Design for NASA Asteroid Redirect Robotic Mission Concept,” 2013.
- [21] J. R. Brophy and B. Muirhead, “Near-earth asteroid retrieval mission (arm) study,” 2013.
- [22] C. Boshuizen, J. Mason, P. Klupar, and S. Spanhake, “Results from the Planet Labs Flock Constellation,” 2014.
- [23] G. Rufino and A. Moccia, “Laboratory Test System for Performance Evaluation of Advanced Star Sensors,” *Journal of Guidance, Control, and Dynamics*, Vol. 25, Mar. 2002, pp. 200–208, 10.2514/2.4888.
- [24] B. G. Boone, J. R. Bruzzi, W. F. Dellinger, B. E. Kluga, and K. M. Strobehn, “Optical Simulator and Testbed for Spacecraft Star Tracker Development,” *Optical Modeling and Performance Predictions II* (M. A. Kahan, ed.), San Diego, California, USA, Aug. 2005, p. 586711, 10.1117/12.619133.
- [25] J. A. Tappe, *Development of Star Tracker System for Accurate Estimation of Spacecraft Attitude*. PhD thesis, Naval Postgraduate School, Monterey, CA, 2009.
- [26] M. A. Samaan, S. R. Steffes, and S. Theil, “Star Tracker Real-Time Hardware in the Loop Testing Using Optical Star Simulator,” *Spaceflight Mechanics*, Vol. 140, New Orleans, Louisiana, Jan. 2011.
- [27] D. Rössler, D. A. K. Pedersen, M. Benn, and J. L. Jørgensen, “Optical Stimulator for Vision-Based Sensors,” *Advanced Optical Technologies*, Vol. 3, 2014, pp. 199–207, 10.1515/aot-2013-0045.
- [28] G. Bradski et al., “The opencv library,” *Doctor Dobbs Journal*, Vol. 25, No. 11, 2000, pp. 120–126.
- [29] C. Beierle, J. Sullivan, and S. D’Amico, “High-Fidelity Verification of Vision-Based Sensors for Inertial and Far-Range Spaceborne Navigation,” *26th International Symposium on Space Flight Dynamics (ISSFD), Matsuyama, Japan, June 3-9, 2017*, 2017.
- [30] F. Markley and D. Mortari, “How to Estimate Attitude from Vector Observations,” *AAS/AIAA Astrodynamics Conference, Girdwood Alaska, August 1619, 1999*, 1999.
- [31] J.-S. Ardaens, S. D’Amico, and O. Montenbruck, “Final Commissioning of the PRISMA GPS Navigation System,” *22nd International Symposium on Space Flight Dynamics*, Sao Jose dos Campos, Brazil, 2014.
- [32] G. Gaias, J.-S. Ardaens, and S. D’Amico, “The Autonomous Vision Approach Navigation and Target Identification (AVANTI) Experiment: Objectives and Design,” *9th International ESA Conference on Guidance, Navigation & Control Systems*, Porto, Portugal, 2014.
- [33] S. D’Amico, *Autonomous Formation Flying in Low Earth Orbit*. PhD thesis, Technical University of Delft, Delft, The Netherlands, 2010.
- [34] D. Eddy, V. Giraldo, and S. D’Amico, “Development and Verification of the Stanford GNSS Navigation Testbed for Spacecraft Formation-Flying,” Technical Note, 2017. URL: https://people.stanford.edu/damicos/sites/default/files/tn2017_eddygiralodamico.pdf.